

Stefan Hayböck¹ & Christian Breitsamter¹

¹Chair of Aerodynamics and Fluid Mechanics, Technical University of Munich, Boltzmannstraße 15, 85748 Garching, Germany; stefan.hayboeck@tum.de, Tel.: +49 89 289 16439

Abstract

Innovative nacelle designs and disruptive technologies are required to minimize drag and weight penalties of high bypass ratio turbofan engines. Active flow control can improve flow quality at the fan-face while significantly reducing structural weight and aerodynamic drag through more aggressive, i.e., shorter inlet geometries. Within the scope of the Lufo VI-2 project AKTIVER, the implementation of active flow control (AFC) on a shortinlet ultra-high bypass ratio (UHBR) engine nacelle is being investigated experimentally and numerically. This paper introduces the generic axisymmetric model, reffered to as SIA (Short-Inlet Active Flow Control)-Nacelle, followed by numerical results of a design concept analysis of the AFC system. Unsteady Reynolds-averaged Navier-Stokes simulations and scale-adaptive simulations are conducted. Analysis of the clean reference case without AFC indicate that large-scale inlet separation starts at an angle of attack of 26°. Here, the primary use case for AFC is at an angle of attack of $\alpha=29^{\circ}$ and a free-stream Mach number of Ma=0.15, which is representative of a take-off roll for strong crosswinds or the wing $C_{L,max}$ condition. The AFC system is tested in continuous and pulsed blowing mode. For the present case, the continuous blowing mode is found to be more effective since pairs of counter-rotating vortices formed by the round jets tend to be more stable. In evaluating the AFC system, significant improvements in inlet performance data are observed compared to the clean configuration. The total pressure coefficient η_{σ} improves by up to 7.1%, the distortion coefficient DC_{60} by 53.0%, and the swirl coefficient SC_{60} by 29.4%.

Keywords: Active Flow Control; Short-Inlet; Nacelle Aerodynamics

1. Introduction

Today's climate policies and social objectives demand a climate-friendly future for aviation. Modern turbofan engines are moving towards higher bypass ratios and larger fan diameters to increase propulsive efficiency through a corresponding reduction in specific thrust. Large bypass ratios and fan diameters of highly fuel-efficient turbofan engines result in higher weight and drag due to a bigger nacelle surface and longer inlet sections. In 1990, Zimbrick and Colehour [1] already discussed the need for shorter than conventional inlets to counteract weight and drag penalties of ultra-high bypass ratio (UHBR) engine nacelles. This, in turn, requires a more compact integration of the fan stage and nacelle than with current turbofan engines. In this context, Peters et al. [2] found a 16% reduction in nacelle drag for a short-inlet design with an inlet length over fan diameter ratio of L/D=0.25compared to the standard configuration with L/D = 0.5. For even shorter inlets, the reduced nacelle drag is associated with a drop in fan efficiency, which is why the authors recommend L/D ratios in the range between 0.25 and 0.4. Aerodynamic limitations for short inlets are the interaction of the fan rotor with over-speed regions at the inlet lip and reduced flow straightening. These mechanisms cause increased flow distortion and reduced fan efficiency relative to conventional inlets. Freeman and Rowe [3] experimentally investigated inlet engine interactions of a large turbofan engine. They found that inlet separation and non-uniform pressure distribution in climb and crosswind conditions

raise the fan operating line, and eventually, the fan could experience rotating stall. Lee et al. [4] performed unsteady simulations under crosswind to analyze aerodynamic instabilities on a modern low-speed fan rig. Inlet separation and a significant loss in stall margin were observed for sufficiently high levels of crosswind. In addition, fan stability was found to be less sensitive to inlet distortion at higher rotational speeds due to flow acceleration upstream of the fan face. Most recently, Piovesan et al. [5] did a detailed analysis of Particle Image Velocimetry (PIV) data for a short-inlet turbofan engine operating under crosswind conditions. Adapting the mass flow contraction ratio (MFCR) allowed achieving different operating conditions with crosswind at fixed velocity. Large-scale diffusion-driven separation dominated at small MFCR, while shock-induced separation was observed at high MFCR.

Active flow control (AFC) can prevent stall and engine surge at off-design conditions by ensuring inflow quality specified by engine manufacturers. The term "active flow control" refers to the introduction of additional energy into the flow through an actuator system, which provides benefits over passive systems [6]. Active control can be deactivated when not needed and adjusted to changing flight conditions. Local air injection with variable frequency at the inlet lip can help to energize and stabilize the boundary layer, increasing the aerodynamic load capacity of engine inlets far beyond current levels. AFC technology has been widely tested on engine inlets, showing great potential. For example, Gorton et al. [7] successfully applied AFC in wind tunnel tests on an S-duct inlet of a blended-wing-body concept aircraft, reducing the inlet distortion value DC_{60} by 84%. Delot et al. [8] experimentally tested continuous and pulsed blowing on a high offset intake diffuser and showed up to 50% improvement in DC_{60} levels. The spatial orientation of the jets, the actuator frequency, and the jet velocity were crucial for the system's overall effectiveness. In a study by Garnier [9], a spectral analysis was carried out on continuous and pulsed supersonic jets in a curved S-duct inlet. Continuous blowing was found to be a more effective operation mode for reattaching the separated flow. According to the author, using the natural frequencies of the uncontrolled, separated flow as actuator frequencies is not recommended. Nambiar and Pachidis [10] did a numerical study on lip blowing on a NASA Common Research Model type engine nacelle at medium to high angles of attack. Continuous circumferential slots in different shapes were located just after the inlet throat, extending 45° on both sides from the nacelle's symmetry plane at the bottom inlet section. Blowing was performed perpendicular to the inlet surface and at an angle of 45°. Wider slots providing a higher mass flow rate and inclined slots were generally found to be more effective than thinner slots blowing perpendicularly. In the paper at hand, a comprehensive numerical study is conducted on a similar engine inlet, analyzing the effect of circular jets in various orientations and arrangements.

Jets in cross-flow (JICF) form complex three-dimensional flows, which have been extensively studied in literature [11–14]. The formation of a counter-rotating vortex pair (CVP) downstream of JICF is crucial for the application in AFC. In his comprehensive work, Margason [12] described the formation of these CVPs in great detail. The pressure distribution at the nozzle exit corresponds approximately to that of a potential flow around a circular cylinder, with stagnation points upstream and downstream and a pressure minimum at the lateral edges. The low pressure leads to a lateral expansion of the jet, while the cross-flow shears the jet fluid downstream along the lateral edges. At increasing distances along the jet path, this shearing causes the downstream face to fold, forming a pair of counter-rotating vortices. Besides the CVP, a horseshoe vortex develops at the nozzle outlet, and a wake vortex street can be observed downstream of the nozzle. Figure 1 provides a sketch of the vortex structures associated with a JICF. The jet centerline path is defined by the locus of the maximum vertical velocity at the symmetry plane.

Three well-established quantities are used to measure the quality of the inlet flow and thus assess the performance of the AFC system. The average total pressure coefficient η_{σ} describes the pressure recovery at the inlet [15, 16]. It is defined as the difference of the average total pressure at the aero-dynamic interface plane (AIP) $p_{t,AIP}$ and the ambient pressure p_{∞} divided by the dynamic pressure of the undisturbed flow $q_{\infty} = 1/2\rho U_{\infty}^2$ (see Eq. 1). Ideally, the value of η_{σ} should be as close to 1 as possible. The distortion coefficient DC_{60} (Eq. 2) is commonly used to evaluate the total pressure distortion at the AIP. It gives the difference between the average total pressure at the AIP $p_{t,AIP}$ and the minimum average total pressure $p_{t,min,60}$ in a segment of 60° at the AIP divided by the average

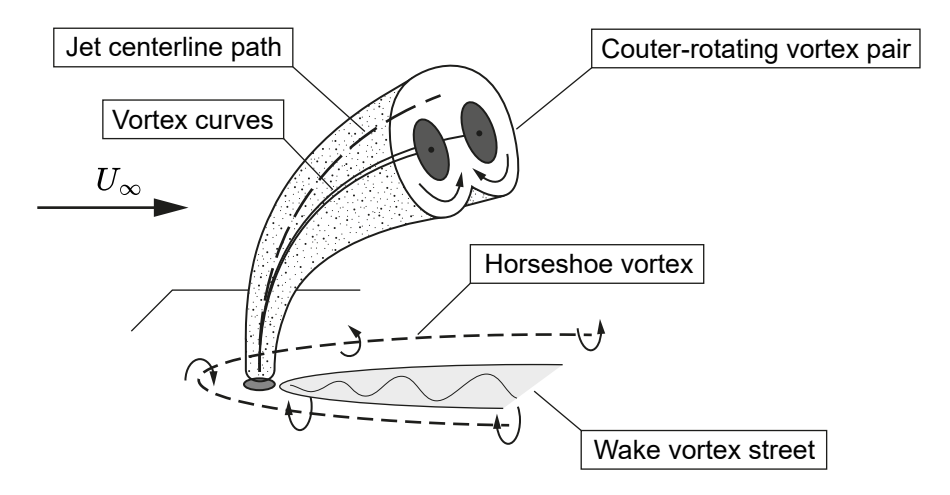


Figure 1 – Sketch of the vortical flow structures associated with a jet in cross-flow, adapted from Margason [12].

dynamic pressure at the AIP q_{AIP} . A secondary effect of flow separation is often a high angular swirl. Guo and Seddon [15] proposed a swirl coefficient SC_{60} (Eq. 3). It is the quotient of the maximum average circumferential velocity $u_{c,max,60}$ in a segment of 60° and the average velocity in x-direction at the AIP u_{AIP} . It is desired to have coefficients DC_{60} and SC_{60} be as small as possible.

$$\eta_{\sigma} = \frac{p_{t,AIP} - p_{\infty}}{q_{\infty}} \tag{1}$$

$$DC_{60} = \frac{p_{t,AIP} - p_{t,min,60}}{q_{AIP}}$$

$$SC_{60} = \frac{u_{c,max,60}}{u_{AIP}}$$
(2)

$$SC_{60} = \frac{u_{c,max,60}}{u_{AIP}} \tag{3}$$

The present paper is structured as follows. In section 2, the SIA (Short-Inlet Active Flow Control)-Nacelle, a generic flow-through nacelle, is introduced, including the chosen approach for the parameterization of the nacelle shape and the characteristics of the AFC system. The numerical setup is explained in section 3, where attention is also given to the validation measures taken. Section 4 provides findings of the design concept analysis. The numerical analysis includes a characterization of the clean configuration without AFC as a reference case. Further, the impact of predefined design parameters on the performance of the AFC system is assessed, and a comprehensive flow analysis of selected designs is carried out. Section 5 summarizes the results and gives an outlook on possible work in the future.

2. Model Design

Within the scope of the Lufo VI-2 project AKTIVER, the implementation of AFC on a short-inlet UHBR engine nacelle is being investigated both experimentally and numerically. Consequently, the model must be designed primarily according to the framework of the low-speed wind tunnel facility A at the Technical University of Munich (TUM). The SIA-Nacelle is a generic, axisymmetric model that reflects the nacelle geometry of modern turbofan engines. The initial design phase neglects possible interactions between a fan and the inlet flow. Thus, the nacelle is designed as a flow-through nacelle for now. In their work on the comparison of powered inlets and flow-through nacelles at high angles of attack, Schulze et al. [17] identified several geometric parameters to control separation onset and the characteristics of the suction peak at the inlet lip of a flow-through nacelle. The design of the SIA-Nacelle incorporates the findings of Schulze et al. to achieve a boundary layer loading similar to powered inlets also on a flow-through nacelle.

2.1 Nacelle Geometry

A custom parameterization tool was developed for the design of the inlet and outer hull of the nacelle, which is based on the Hybrid intuitive Class Shape Transformation (HiCST) from Christie et

Table 1 – List of characteristic parameters used for the generic axisymmetric nacelle geometry.

Parameter	Formula	Description	Value
AR_{nac}	l_{nac}/r_{hl}	aspect ratio of the nacelle	2.759
$f_{r,max}$	r_{max}/r_{hl}	maximum radius	1.175
f_{max}	l_{max}/l_{nac}	location of max. radius	0.3
eta_{te}	_	boattail angle	8.0°
f_{nose}	r_{nose}/r_{hl}	nose radius of cowling	0.04
f_{te}	r_{te}/r_{hl}	trailing edge radius	1.0
$f_{r,fan}$	r_{fan}/r_{hl}	fan radius	0.948
f_{il}	$r_{il} \cdot b/a^2$	initial lip radius of inlet	0.45
L/D	l_{int}/d_{fan}	length diameter ratio	0.35
$f_{\kappa,th}$	$\kappa_{th} \cdot r_{hl}$	curvature at throat	5.0
γ_{fan}	_	wall angle at fan	-3.0°
$f_{\kappa,fan}$	$\kappa_{fan} \cdot r_{hl}$	curvature at fan	-1.0
AR	b/a	inlet aspect ratio	2.0
CR	$(r_{hl}/r_{th})^2$	inlet contraction ratio	1.2

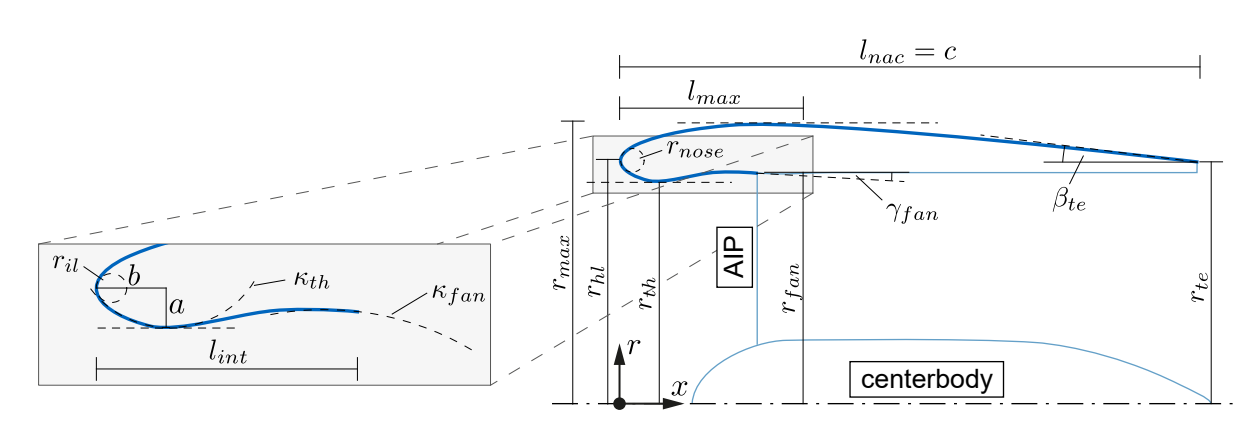


Figure 2 – Display of the characteristic metrics used in the parameterization tool. The zoom window gives a detailed view of the inlet section.

al. [18, 19]. Kulfan and Bussoletti [20] pioneered this method by mathematically representing the shapes of aircraft components. Instead of using a large number of coordinates, a simple class function of the form $C(x/c) = \sqrt{x/c} \cdot (1-x/c)$ represents the rough geometry, and a shape function defines arbitrary 2D and 3D geometries. To fully describe the smooth profile curve of a dimensionless, axisymmetric nacelle geometry, 14 characteristic parameters are needed. The fan radius r_{fan} is an extra, dimensionally dependent parameter that determines the spatial extension of the nacelle. Table 1 lists all dimensionless parameters along with their formula definitions, descriptions, and chosen values for the SIA-Nacelle. The parameterization tool uses characteristic metrics of an engine nacelle, illustrated in Fig. 2. These parameters closely represent the shape of nacelles on short-inlet turbofan engines. The inlet length over fan diameter ratio L/D is 0.35, which is significantly lower than typical L/D ratios of current long-range aircraft engines. More characteristic inlet parameters are the lip aspect ratio of AR = 2.0 and the inlet contraction ratio of CR = 1.2. There are two main differences in the inlet geometry of the SIA-Nacelle compared to existing powered inlets: (i) an increased curvature at the throat, which leads to an increasing negative camber of the profile and premature flow separation towards lower angles of attack, and (ii) a bump upstream of the AIP. This bump serves as a useful means to create a recovery in the flow, preventing the separation bubble from breaking up over a larger stretch in angle of attack. The section between the AIP and the trailing edge of the nacelle is defined by a constant inner diameter d_{fan} . The SIA-Nacelle also features a centerbody in its core, designed to attach instrumentation, such as a traversable total pressure rake or an unsteady multi-hole probe, in future wind tunnel campaigns.

To determine the size of the nacelle, two criteria were taken into consideration: (i) the largest model size is advantageous to address large Reynolds numbers in wind tunnel tests and provide sufficient installation space for instrumentation, and (ii) the maximum size of the model is limited by the blockage of the measurement section in the wind tunnel. The maximum blockage should be kept below 10%. Thus, the fan radius is set here to $r_{fan} = 0.275$ m, which results in a radius at the highlight r_{hl} of 0.29 m and a nacelle chord length $c = l_{nac}$ of 0.8 m.

2.2 Flow Control Characteristics

The AFC system can be characterized by eight design parameters. The diameter of the blowing ports depends on the jet diameter ratio d_{jet}/d_{fan} , which is the only constant parameter at a value of 0.473. This gives a jet diameter of 2.6 mm at the blowing port. The number of circular blowing ports and their circumferential distribution at the inlet are determined by the parameters N_{iet} and the spacing angle θ_{jet} . The AFC system covers approximately a circumferential angle of $\theta_{AFC} \approx 108^{\circ}$ at the lower inlet lip for all chosen blowing port numbers and the corresponding angular spacing. The parameter x_{iet}/l_{inl} sets the position of the blowing ports along the x-axis relative to the total inlet length. For ecample, the throat is located at 26.25% of the inlet length. The pitch angle α_{iet} defines the inclination of the jets with respect to the local surface in the radial rx-plane. A pitch angle of $\alpha_{iet}=90^{\circ}$ implies a jet in the direction of the surface normal. For practical reasons, the smallest possible pitch angle is set to 70°. The jet momentum and time characteristics of the jet are specified by the velocity ratio U_{jet}/U_{∞} , the pulse frequency f_{pulse} and the duty cycle DC_{pulse} . The duty cycle of a periodic pulse sequence $DC_{pulse} = \tau/T$ indicates the ratio of the pulse duration τ to the period duration T. Table 2 displays all parameters of the AFC system and all values tested for this paper. A visual representation of the SIA-Nacelle in the half-model configuration with a close-up view of the AFC system is shown in Figure 3.

Table 2 – List of parameters introduced to characterize the AFC system.

Parameter	Description	Unit	Tested Values
d_{jet}/d_{fan}	jet diameter ratio	[%]	0.473 (constant)
N_{jet}	number of jets	[1]	[24, 28, 32, 36]
$ heta_{jet}$	spacing angle	[°]	[3.1, 3.5, 4.0, 4.7]
x_{jet}/l_{int}	jet location in x-direction	[%]	[20.0, 25.0, 27.5, 30.0, 32.5, 35.0]
$lpha_{jet}$	pitch angle	[°]	[70, 75, 80, 85, 90]
U_{jet}/U_{∞}	jet velocity ratio	[1]	[0.5, 1.0, 1.5, 2.0, 2.5]
f_{pulse}	pulse frequency	[Hz]	[0, 48, 96, 162]
DC_{pulse}	pulse duty cycle	[%]	[25, 50]

3. Numerical Method

To keep the numerical cost within acceptable limits, an Unsteady Reynolds-averaged Navier-Stokes simulations (URANS) approach is chosen for analysis of the clean configuration and the design analysis of the AFC system. Based on a symmetric flow field assumption, only a half-model of the SIA-Nacelle is simulated. A Scale-Adaptive Simulation (SAS) method is employed for scale-resolving simulations to analyze the temporal features of the flow. In their work, Egorov et al. [21] demonstrate the improved prediction of highly separated flows and increased accuracy in the time/frequency domain of the SAS method compared to simple URANS approaches. Since the same turbulence model is used in both simulation methods, the method has a minor influence on the separation line.

3.1 Numerical Setup

All computations are conducted with the pressure-based flow solver ANSYS Fluent 23R1 using a finite volume method to solve the incompressible Navier-Stokes equations. A steady RANS result serves as an initial solution for both URANS and scale-adaptive simulations. The SIMPLE algorithm links pressure and velocity, while a momentum-based Rhie-Chow method is employed for mass flux.

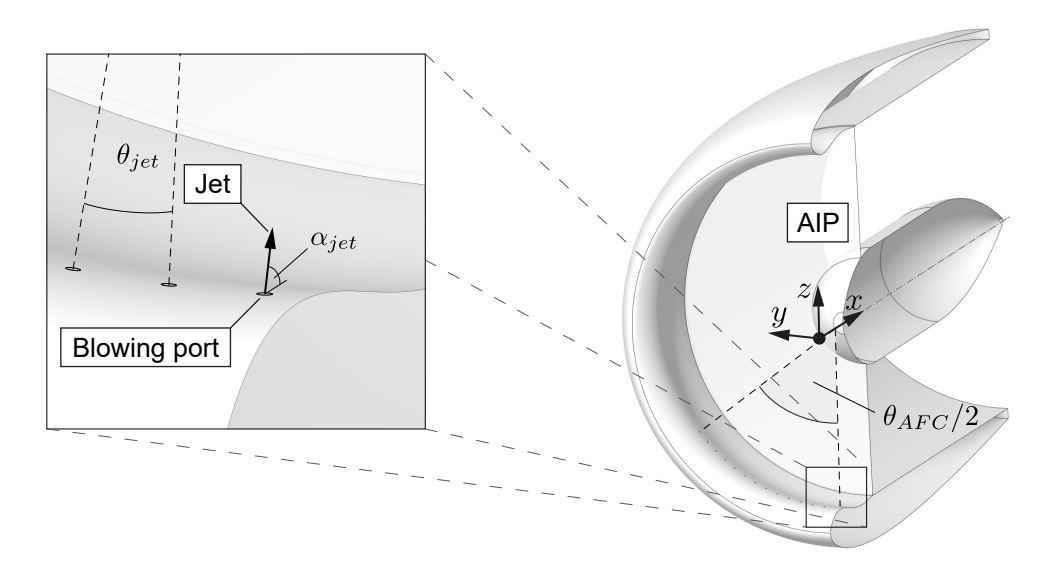


Figure 3 – Illustration of the AFC system of the SIA-Nacelle with a close-up view of the lower inlet section.

Convection and diffusion terms in the conservation equations are discretized by a least squares cellbased method. Second-order accurate schemes discretize pressure and the turbulence variables k and ω , while the momentum equation is solved using a bounded central differencing method. Timedependent calculations are performed by a bounded second-order implicit formulation. The fixed time-step size is set to 1 · 10⁻⁴ s for simulations of the clean configuration and AFC in continuous blowing mode, allowing a maximum of 100 inner iterations per time-step. For simulations of pulsed blowing, an additional timestep criterion is introduced requiring at least 300 time steps per blowing cycle. The Cauchy convergence criterion is specified for the lift and drag coefficients C_L and C_D , reaching convergence if both integral values meet 5 · 10⁻⁶ over a stretch of 4 iterations. The total simulation time is at least 0.5 s, with data sampling for time statistics enabled at 0.1 s. Unless otherwise specified, the following results display the averaged values over time. The Courant number is calculated to be CFL = 3.2 based on the fixed time-step chosen for the clean configuration and AFC in continuous blowing mode. A time-step independence study confirms sufficient temporal resolution, as an implicit transient formulation eliminates the need for a strict CFL < 1 criterion. The maximum relative error is less than 0.2% when comparing integral force coefficients and the total pressure coefficient for CFL values of 3.2 and 0.8.

The numerical setup is validated against experimental data of a flow-through nacelle provided by Schulze and Kähler [22]. After conducting a preliminary grid convergence study on the geometry from Schulze and Kähler, RANS simulations compare the c_p -curves obtained from different turbulence models with experimental data. The c_p -curve is evaluated at the keel line of the nacelle. The chosen angle of attack for validation is $\alpha = 23.5^{\circ}$, which falls within the range where the onset of flow separation occurs at the bottom inlet lip. The comparison of turbulence models is depicted in Fig. 4a. The Generalized K- ω (GEKO)-1.0 model accurately predicts separation behavior and reproduces the suction peak at the bottom inlet lip in good agreement with the experiment. Variants of the GEKO two-equation model differ in the value of the separation parameter C_{SEP} , one of six free parameters available to the user for adjusting the turbulence model without affecting the basic calibration of the model [23]. All simulations presented below use the K-ω GEKO-1.0 turbulence model. The computational grid of this study is created with the ANSYS Fluent Meshing grid generator. A Poly-Hexcore grid structure combines high-quality octree hexahedron cells in the bulk region with isotropic polyprisms in the boundary layer. To ensure proper capture of crucial flow features, refinement regions are designated inside the nacelle, at the bottom inlet section, in the mixing zone of the jets, and in the wake. The surface mesh shows high levels of detail at the nacelle's leading and trailing edge and at the blowing ports. The boundary layer is resolved using 33 prism layers, a first cell height of 0.0035 mm, and a stretching ratio of 1.2, resulting in a y^+ -value of $y^+ < 1$ for the entire domain. The

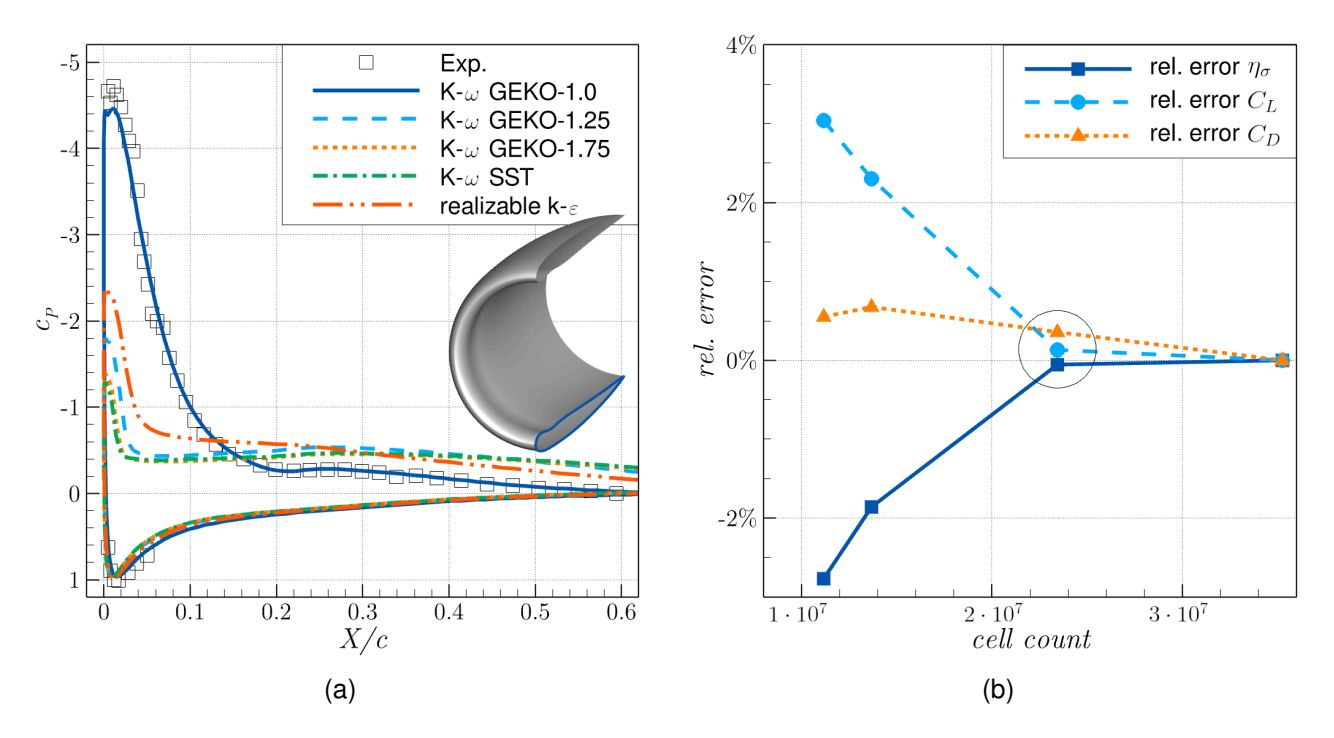


Figure 4 – (a) c_p -curves simulated with different turbulence models compared with experimental data from Schulze and Kähler [22] at $\alpha=23.5^\circ$ and $Re_c=1.34\cdot10^6$; (b) Result of the grid convergence study in continuous blowing mode with four different grid sizes.

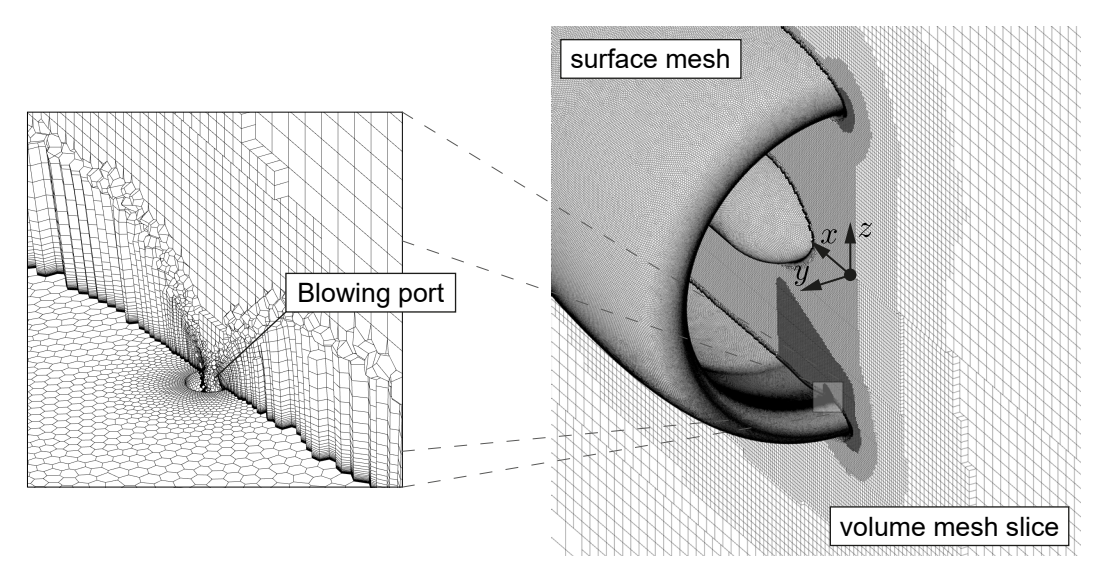


Figure 5 – Poly-Hexcore grid structure of the chosen grid size with a detailed view of the surface mesh and the volume mesh slice at the blowing port.

grid size is determined by a grid convergence study in continuous blowing mode. Decisive parameters are the time-averaged integral lift and drag coefficient C_L and C_D , as well as the time-averaged total pressure coefficient η_σ . The surface and volume mesh is gradually refined for four different grid sizes, while the first cell height and the number of prism layers remain unchanged. Figure 4b plots the error of the force coefficients and the total pressure coefficient relative to the finest mesh with 35.3 million cells when using the mesh sizes coarse, medium, fine, and extra-fine. The fine mesh with around 23.4 million cells is the most appropriate option as it has a relative error below 0.4% for all decisive quantities. Figure 5 depicts the grid structure of the final grid, featuring a polyhedral surface mesh, poly-prisms in the boundary layer and hexahedra in the bulk region. The zoom window shows the very fine grid resolution in areas of the blowing ports and the mixing zones of the jets. A symmetry boundary condition confines the fluid domain in the xz-plane. Velocity inlet boundary con-

ditions with velocity components $u=U_\infty\cdot cos(\alpha)$ and $w=U_\infty\cdot sin(\alpha)$ and a pressure-outlet boundary condition represent the outer boundaries of the domain. The turbulence intensity is set to 1%. The box-shaped computational domain measures $60c\times20c\times40c$ (length×width×height), with the nacelle placed 20 chord lengths downstream of the front face and 20 chord lengths above the bottom face of the domain. The jet nozzles leading to the blowing ports are modeled as cylindrical channels with a length of 3 mm, where a realistic boundary layer builds up. To specify the jet velocity, a velocity inlet boundary condition represents the inflow of the channels.

3.2 Flow Control Use Case

This paper focuses on the AFC use case in the high angle of attack range. For instance, the wing's $C_{L,max}$ condition is crucial in the certification process, with an anticipation of high levels of turbulence and flow separation. The corresponding angle of attack of the engine inlet is taken from Peters et al. [2] and is set to $\alpha=29^{\circ}$. Engine nacelles typically encounter higher angles of attack than the wing because of the upwash effect of the wing. Due to the inlet's axisymmetric design, crosswind and angle of attack can be combined and represented by a single angle, α . For the purpose of simplicity, the angle α is only referred to as angle of attack in the following. The free-stream Mach number is fixed at $Ma_{\infty}=0.15$ for all simulations. This value is governed by the highest achievable test section velocity in future wind tunnel tests at Wind Tunnel A of the Chair of Aerodynamics and Fluid Mechanics of the Technical University of Munich. The take-off roll in strong crosswinds is an example use-case scenario where acceptable Reynolds number similarity can be achieved despite a low Mach number.

4. Results and Discussion

All results shown are based on simulations conducted at a Mach number of $Ma_{\infty}=0.15$. The Reynolds number calculated with the chord length of the nacelle gives $Re_c=2.79\cdot 10^6$, which corresponds to a free-stream velocity of $U_{\infty}=51$ m/s. If not otherwise stated, results are calculated from time-averaged simulation data.

4.1 Clean Reference Case

A comprehensive numerical analysis of the clean configuration without AFC serves as a reference for evaluating the performance of the flow control system. Figure 6a shows the behavior of the three performance metrics η_{σ} , DC_{60} and SC_{60} across the angle of attack range $21^{\circ} \le \alpha \le 30^{\circ}$ computed from GEKO-URANS simulations. All three curves display a "discontinuity" between the angles of attack of 25° and 26°, with the quantities η_{σ} and DC_{60} showing a significant step. Figures 6b and 6c, in which the size of the turbulent recirculation zone is visualized by the iso-surface $u/U_{\infty}=0$ and the non-dimensional total pressure at the AIP is displayed, give reason for this discontinuity. Starting at $\alpha = 22^{\circ}$, a closed turbulent separation bubble forms downstream of the inlet throat, which then recovers quickly upstream of the AIP due to the bump described in section 2.1. The closed separation bubble has a minor impact on the inlet flow, as performance values show only small changes. It expands as the angle of attack increases and eventually breaks up at $\alpha=26^{\circ}$. Consequently, the separation region suddenly extends over a large portion of the chord length, causing a significant total pressure loss at the AIP. The loss in total pressure at the AIP is mainly reflected in values of η_{σ} and DC_{60} . However, the swirl coefficient SC_{60} also increases disproportionally due to the influence of large scale flow separation. As the angle of attack increases further, the separation region continues to expand both axially and circumferentially, eventually reaching the trailing edge of the nacelle at $\alpha=28^{\circ}$. The reference angle chosen for evaluating the AFC system is $\alpha=29^{\circ}$. Figure 7a illustrates the inlet separation and the total pressure loss at the AIP from the GEKO-URANS simulation at 29°. The recirculation region significantly increases compared to Fig. 6c at 26°, and the area of high total pressure loss at the AIP also expands radially and circumferentially. Thus, the reference values $\eta_{\sigma,ref}=0.85$, $DC_{60,ref}=0.46$ and $SC_{60,ref}=0.24$ result for the performance metrics at $\alpha=29^{\circ}$. An additional scale-adaptive GEKO-SAS simulation at 29° is conducted to analyze the time and frequency domain of the clean reference case. A numerical time step of 4 · 10⁻⁵ s gives a Nyquist frequency of 12500 Hz. Figure 7b displays the Power Spectral Density (PSD) of the normalized x-velocity fluctuations u'/\overline{u}_{MP} for monitor points MP1 and MP2. The plot includes the corresponding Strouhal number

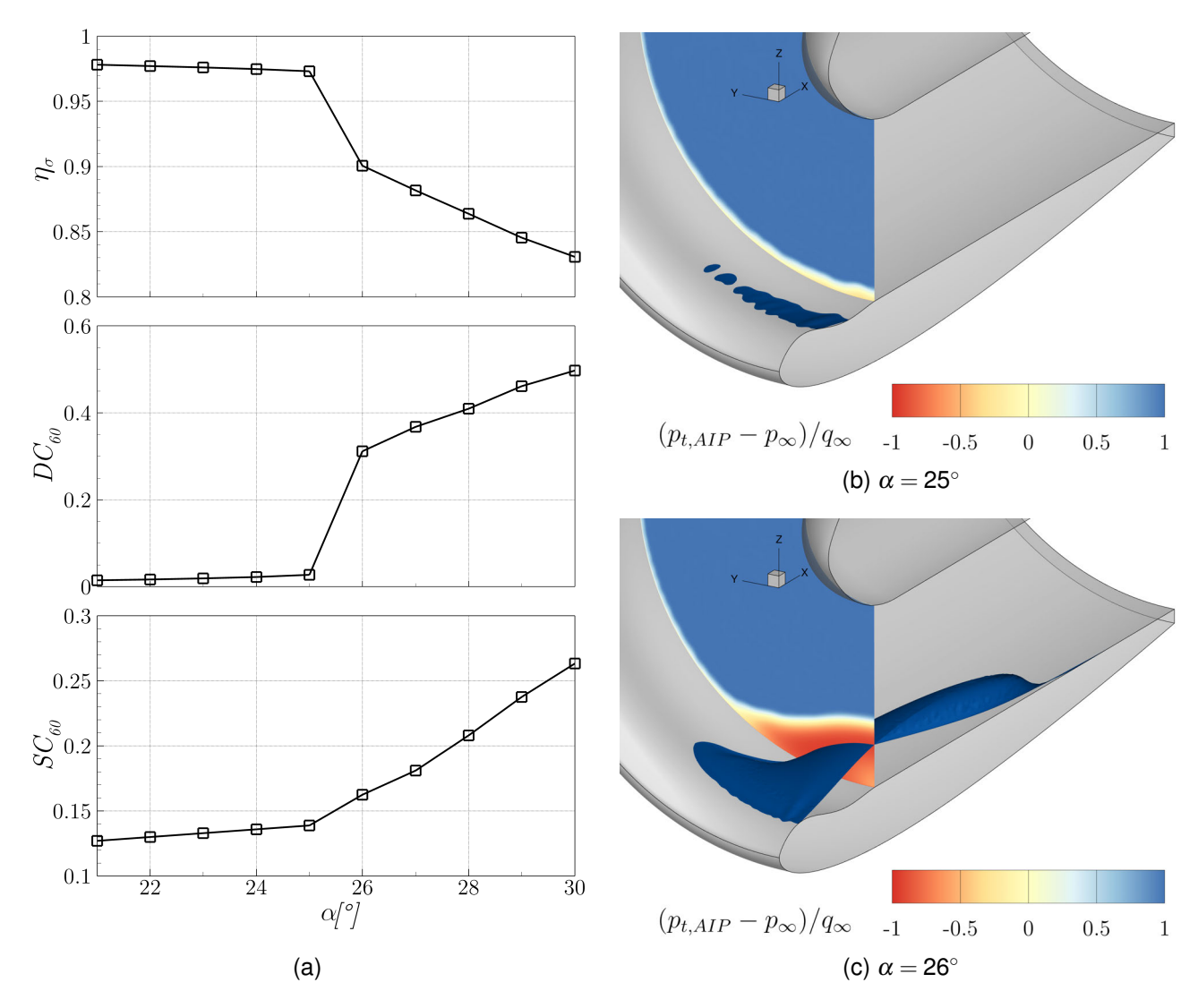


Figure 6 – (a) Polar diagrams of the three performance metrics η_{σ} , DC_{60} and SC_{60} for angles of attack $21^{\circ} \leq \alpha \leq 30^{\circ}$; Plot of the recirculation zone at the bottom inlet lip visualized by the iso-surface $u/U_{\infty}=0$ and the non-dimensional total pressure at the AIP at (b) $\alpha=25^{\circ}$; and (c) $\alpha=26^{\circ}$.

Sr, calculated from the highlight diameter d_{hl} and the inflow velocity U_{∞} . The position of the monitor points is indicated in Fig. 7a, with MP1 located in the xz symmetry plane of the SIA-Nacelle and MP2 on the AIP. The spectral analysis of the clean configuration can provide information on whether dominant frequencies already prevail in the flow without any flow control system in use. MP1 experiences significantly higher velocity fluctuations, leading to a higher power density compared to MP2 across the entire frequency range. While the spectrum of MP1 exhibits two frequency peaks at around 350 Hz and 700 Hz, the spectrum of MP2 only shows a slight peak at 350 Hz. The origin of these high-frequency peaks has yet to be fully clarified and will be investigated in more detail after the first experimental campaign. There are no sharply defined frequency peaks in the low-frequency range below 100 Hz, where vortex-shedding frequencies are typically expected. This is consistent with the findings of Schulze [24], who conducted unsteady PIV and surface pressure measurements for the frequency analysis of a stalling flow-through nacelle.

4.2 Continuous Blowing Mode

All results for AFC in continuous blowing mode presented in this section and those for pulsed blowing mode in section 4.3 are obtained from simulations at an angle of attack of 29°. The variation of geometric parameters of the AFC system and the jet velocity is only performed in continuous blowing mode. The requirements for temporal discretization (small time step size) and, consequently, the computational costs rise significantly in pulsed blowing mode. Selected values for the blowing fre-

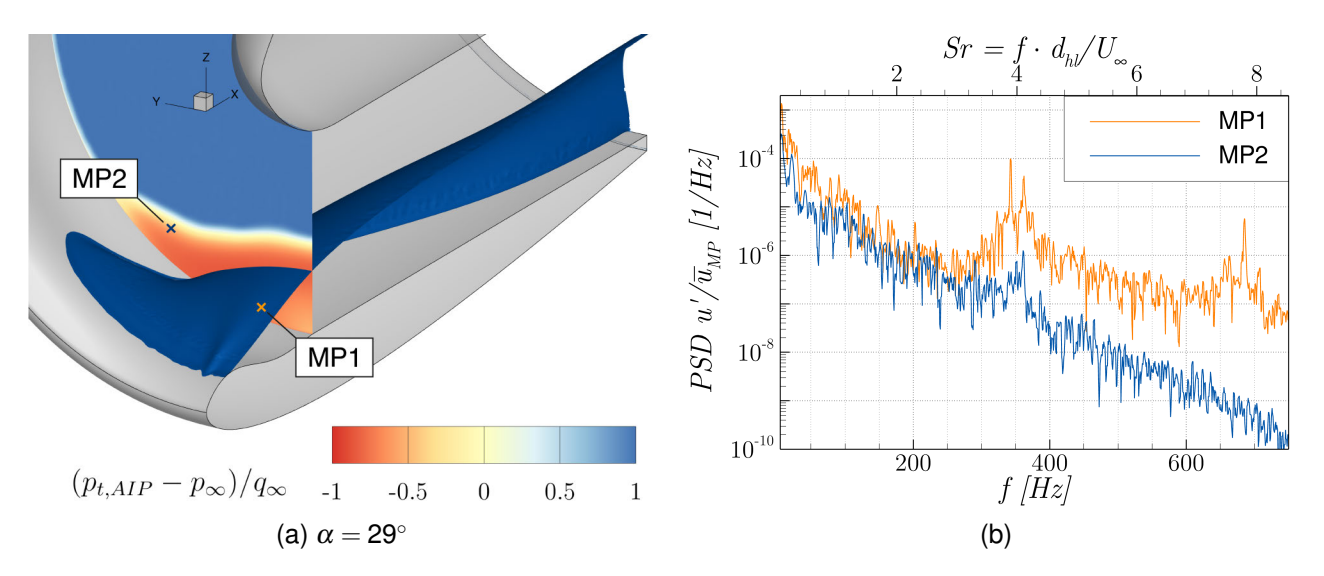


Figure 7 – (a) Plot of the recirculation zone at the bottom inlet lip visualized by the iso-surface $u/U_{\infty}=0$ and the non-dimensional total pressure at the AIP at $\alpha=29^{\circ}$ (GEKO-URANS); (b) corresponding plot of the power spectral density of the normalized x-velocity fluctuation u'/\overline{u}_{MP} at monitor points 1 and 2 (GEKO-SAS).

quency and duty cycle are later tested on a fixed geometry with fixed jet velocity ratio. The starting point of each parameter variation is the baseline configuration of the AFC system, which was specified in preliminary tests. The parameter vector \vec{g}_{bsl} fully describes the baseline configuration (see Eqn. 4).

$$\vec{g}_{bsl} = \begin{bmatrix} d_{jet}/d_{fan} \\ N_{jet} \\ \theta_{jet} \\ x_{jet}/l_{int} \\ \alpha_{jet} \\ U_{jet}/U_{\infty} \\ f_{pulse} \\ DC_{pulse} \end{bmatrix} = \begin{bmatrix} 0.473\% \\ 28 \\ 4^{\circ} \\ 30.0\% \\ 90^{\circ} \\ 2.0 \\ 0 \text{ Hz} \\ - \end{bmatrix}$$

$$(4)$$

A comparison of the performance metrics of the baseline and clean configurations demonstrates the significant improvement that AFC can bring to the inlet flow under off-design conditions. The total pressure coefficient improves by 7.1% to a value of $\eta_{\sigma,bsl} = 0.91$. The distortion coefficient shows an even greater improvement of 53.0% to a value of $DC_{60,bsl} = 0.22$, and the swirl coefficient decreases by 29.4% to a value of $SC_{60,bsl} = 0.17$. Figure 8a shows the instantaneous vortex structures of the baseline configuration at t = 0.7 s through the Q-criterion computed with the scale-resolving GEKO-SAS model. The color scale of the plot depicts the non-dimensional total pressure according to the legend in Fig. 8b. In Fig. 8a, the ability of the GEKO-SAS model to resolve the turbulent structures in the separation region is demonstrated. Further, it shows the changing development of vortex structures depending on the circumferential angle. Vortex structures with low total pressure form at the lower inlet lip near the symmetry plane and in a small conical zone downstream of the 12th blowing port. Figure 8b illustrates the separation bubble and the non-dimensional total pressure at the AIP, similar to the clean reference case in Fig. 7a. The comparison indicates that applying AFC in continuous blowing mode significantly decreases the recirculation zone; thus, the area of total pressure loss at the AIP is visibly smaller. The combination of AFC in continuous blowing mode and the complex three-dimensional inlet shape causes the recirculation zone to split into two counter-rotating systems. An analysis of surface streamlines on the nacelle reveals that the large recirculation area near the symmetry plane rotates clockwise, while the smaller recirculation area at the outer blowing ports rotates counter-clockwise. The split occurs downstream of ports 10 and 11 (count starting at symmetry plane), where high axial velocities prevail.

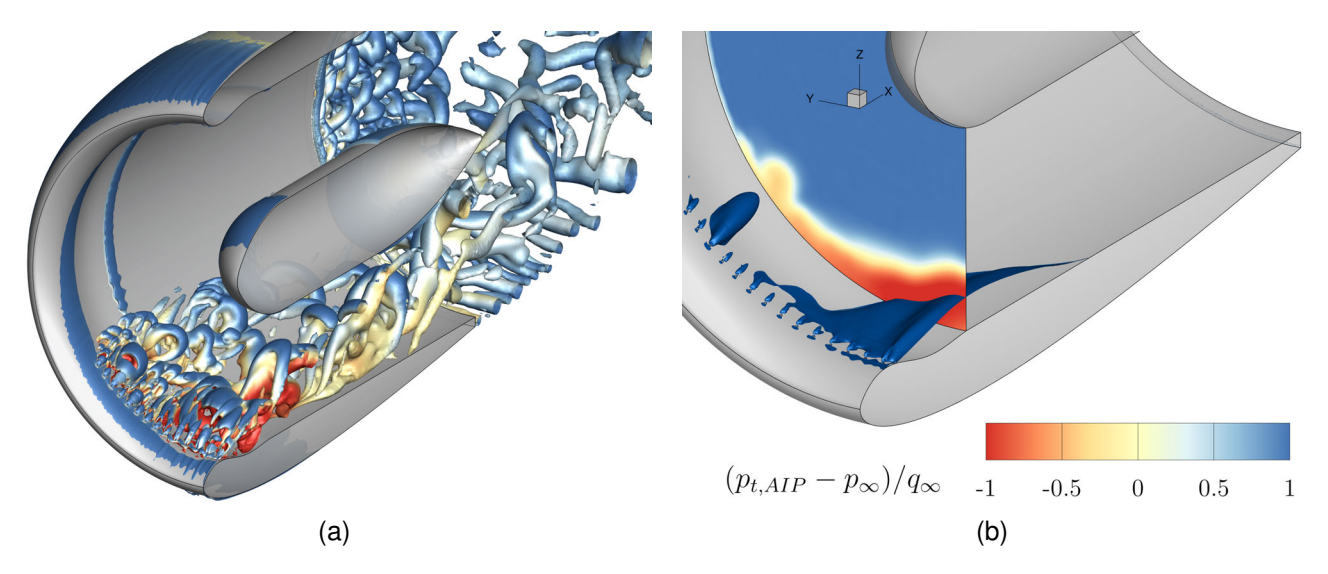


Figure 8 – Flow field of the baseline configuration at $\alpha=29^{\circ}$ and $Re_c=2.79\cdot 10^6$: (a) Instantaneous vortex flow of a scale-resolving GEKO-SAS simulation visualized by the iso-surface of the Q-criterion, $Q=10^5$ s⁻²; (b) Plot of the time-averaged recirculation zone at the bottom inlet lip visualized by the iso-surface $u/U_{\infty}=0$ and the non-dimensional total pressure at the AIP.

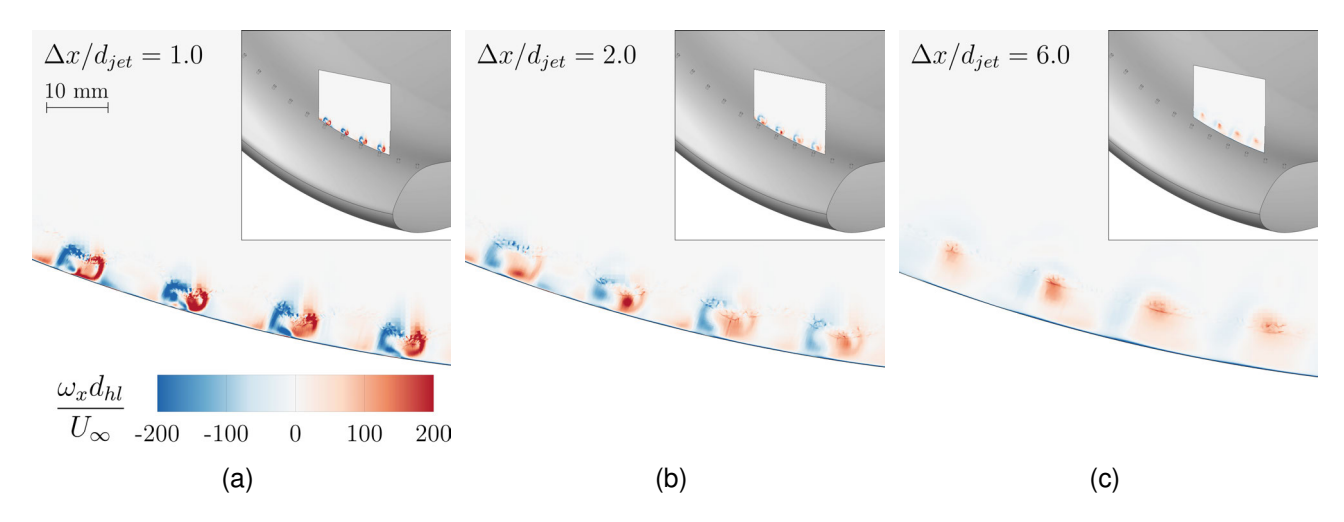


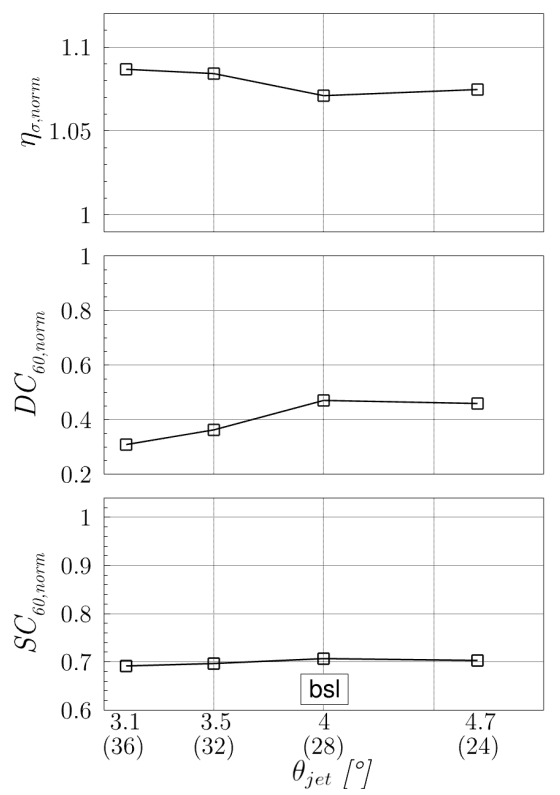
Figure 9 – Plot of the time-averaged normalized x-vorticity at different x-positions downstream of blowing ports 3-6: (a) $\Delta x/d_{jet} = 1.0$; (b) $\Delta x/d_{jet} = 2.0$; and (c) $\Delta x/d_{jet} = 6.0$.

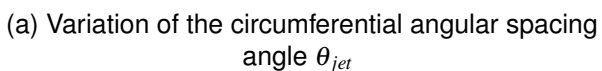
Figure 9 shows the formation of counter-rotation vortex pairs downstream of blowing ports 3-6, as outlined in section 1. The graph displays the normalized x-vorticity for x-slices at distances $\Delta x/d_{jet} = 1.0$, 2.0 and 6.0 from the port center. As the shear layer of the jet starts to coil and convection with the main flow begins, the CVPs are visible as coherent vortex structures at a distance of $\Delta x/d_{iet} = 1.0$. The vortices stimulate the transport of momentum close to the wall, leading to an energized boundary layer and delayed flow separation. The given scaling in Fig. 9a suggests a spatial extension of the CVPs in the range of 10 mm. The downstream x-slices at distances $\Delta x/d_{jet} = 2.0$ and 6.0 indicate that the maximum vorticity in the vortex core decreases as the distance from the blowing port increases. It is evident that the stability and form of these vortices is influenced by the local flow direction of the main flow. For example, vortex axes of CVPs located near the symmetry plane show a lager distance from the model surface, as the highest radial velocities occur near the recirculation zone at the inlet bottom. Due to swirling flows with high circumferential velocity, clockwise-rotating vortices (positive vorticity) appear to be more stable than counter-clockwiserotating vortices. The recirculating flow downstream of the CVPs counteracts the high axial velocities in vortex cores and causes the vortices to dissipate faster. However, the comparison between the clean and baseline configurations reveals a significant improvement in the inlet flow due to the CVPs.

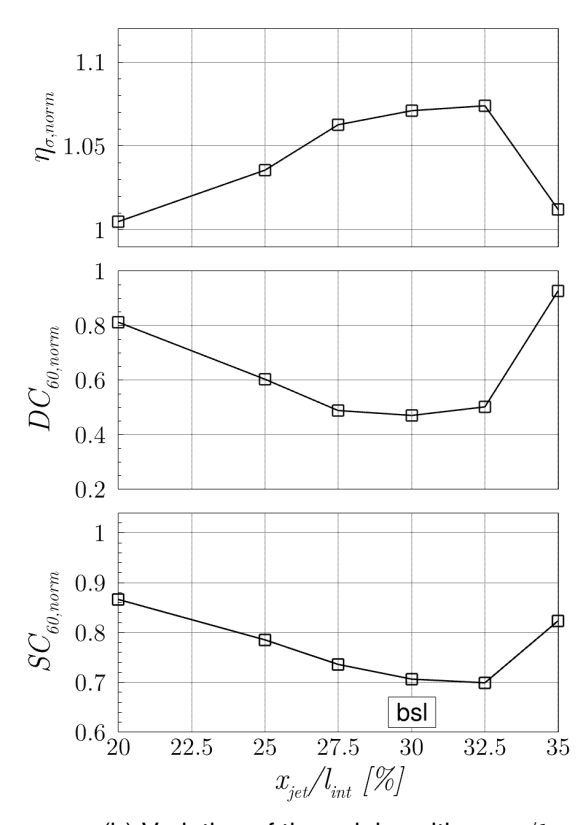
Starting from the baseline configuration characterized above, the five parameters N_{jet} , θ_{jet} , x_{jet}/l_{int} , α_{jet} and U_{jet}/U_{∞} are altered in GEKO-URANS simulations to assess their respective influence on the performance of the AFC system. The parameters N_{jet} and θ_{jet} are linked such that the AFC system covers a constant circumferential angle $\theta_{AFC} = (N_{jet} - 1) \cdot \theta_{jet} \approx 108^{\circ}$. In Fig. 10, the performance metrics η_{σ} , DC_{60} and SC_{60} are given in a normalized form, using the corresponding reference value of the clean configuration as normalization value. For any evaluation quantity (*) applies $(*)_{norm} = (*)/(*)_{ref}$. Figure 10a shows the change in performance data when the circumferential spacing angle of the blowing ports θ_{jet} is varied. The number of blowing ports N_{jet} used for the respective angle is indicated in brackets in the diagram. Data shows a consistent trend among all evaluation variables. The same is true for the variation of all variables. All evaluation quantities, thus the overall performance of the AFC system, improve towards smaller angular spacing. The relative change in $\eta_{\sigma,norm}$ and $SC_{60,norm}$ with respect to the baseline numbers is only minimal. However, achieving the best $DC_{60,norm}$ value of all variations at $\theta_{iet} = 3.1$ with 36 blowing ports is noteworthy. This is primarily due to the higher number of blowing ports, injecting a higher overall mass flow and, hence, more energy into the main flow. Figure 10b depicts the change in performance data resulting from different relative x-position of the blowing ports x_{iet}/l_{int} . Data indicates that the greatest improvements can be made at positions 30% and 32.5% of the inlet length. Since the inlet throat is located at 26.25% of the inlet length, the desired position is downstream of the throat. An analysis of the flow field reveals that CVPs also form when blowing is performed upstream of the throat. The separation line also moves upstream, which causes the recirculation zone to expand and split into three large regions. If blowing occurs downstream of 32.5%, the AFC system also loses performance, as indicated by the numbers of 35%. In this case, the separation line is, for the most part, already in front of the blowing ports, preventing the formation of high x-vorticity CVPs. Figure 10c plots the data with variable pitch angle α_{jet} . The simulated data indicates best performance with blowing almost normal to the local surface at 85°-90° pitch angle. Smaller pitch angles complicate the formation of CVPs, as the shear layer roll-up is suppressed. At $\alpha_{jet} = 75^{\circ}$, the AFC system loses its performance almost completely, as the recirculation zone can only be slightly narrowed at the outer blowing ports. The increasing performance at $\alpha_{iet} = 70^{\circ}$ can be explained by a change in the working principle of the AFC system. Momentum is now gained directly via tangential blowing rather than being transported to the wall by a vortex. Last, Fig. 10d illustrates how the AFC system performance is affected by the jet velocity ratio U_{jet}/U_{∞} . The results indicate that velocity ratios up to a value of 1 have little or no positive impact. Subsequently, the performance data improves continuously as the velocity ratio increases, with $\eta_{\sigma,norm}$ and $DC_{60,norm}$ reaching peak values for $U_{jet}/U_{\infty}=2.5$. The higher velocity ratio provides higher mass flow and more stable CVPs with high axial velocities. Recirculation can almost entirely be avoided except for a small region near the symmetry plane.

4.3 Pulsed Blowing Mode

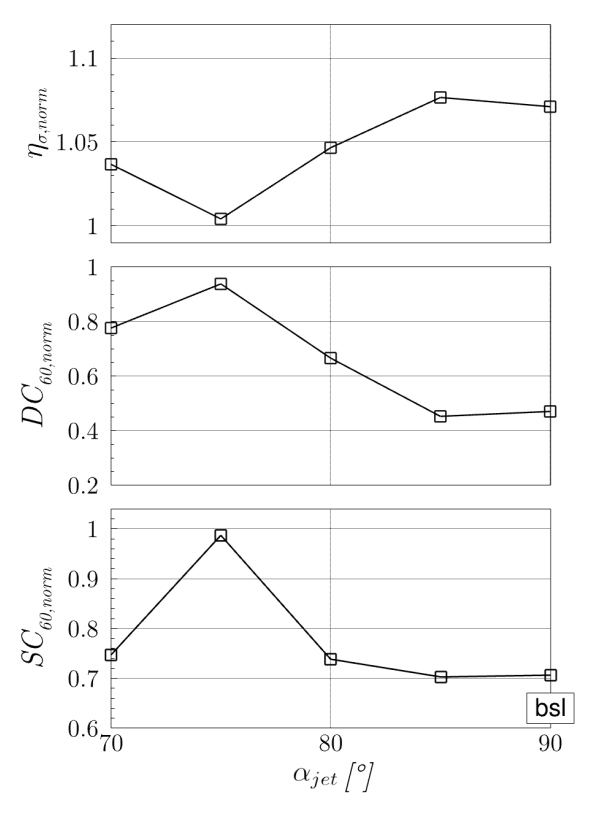
After analyzing the influence of geometric parameters and the velocity ratio in the preceding lines, this subsection is dedicated to the temporal characteristics of the AFC system. It is defined by the blowing frequency f_{pulse} and the duty cycle DC_{pulse} . To ensure better comparability with other AFC parameters, the baseline configuration is once again used for all geometry parameters and the velocity ratio. The analysis in pulsed blowing mode only presents the results of the scale-resolving GEKO-SAS simulations. Figure 11a provides, similarly to Fig. 10, the progression of the performance metrics at different pulse frequencies and duty cycles. During preliminary GEKO-URANS simulations, a duty cycle of $DC_{pulse} = 25\%$ consistently performed worse than 50%. Therefore, only a duty cycle of 50% is used for the scale-resolving simulations, except at $f_{pulse} = 96$ Hz. The plots in Fig. 11a indicate that the values for the normalized total pressure coefficient $\eta_{\sigma,norm}$ and the normalized distortion coefficient $DC_{60,norm}$ deteriorate across all frequencies compared to continuous blowing $(f_{pulse} = 0 \text{ Hz})$. Nevertheless, the results still show an improvement compared to the clean configuration, which slightly increases at higher frequencies. In contrast, the normalized swirl coefficient SC_{60,norm} remains consistent at the same level as for continuous blowing, regardless of the pulse frequency. Thus, the results suggest pulsed blowing is equally efficient at preventing swirl as continuous blowing. The comparison of the two duty cycles at a pulse frequency of 96 Hz confirms that a duty cycle of $DC_{pulse} = 25\%$ does not improve the performance metrics $\eta_{\sigma,norm}$ and $DC_{60,norm}$ relative to the



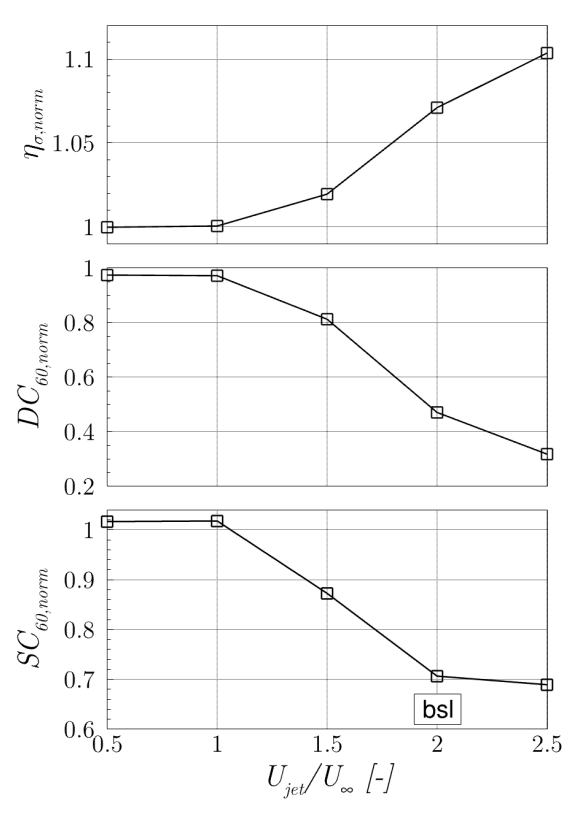




(b) Variation of the axial position $x_{\it jet}/l_{\it int}$



(c) Variation of the pitch angle α_{jet}



(d) Variation of jet velocity ratio $U_{\it iet}/U_{\infty}$

Figure 10 – Result of the variation of selected AFC system parameters, quantified by the performance metrics $\eta_{\sigma,norm}$, $DC_{60,norm}$ and $SC_{60,norm}$. All of the constant parameters correspond to the baseline configuration (bsl).

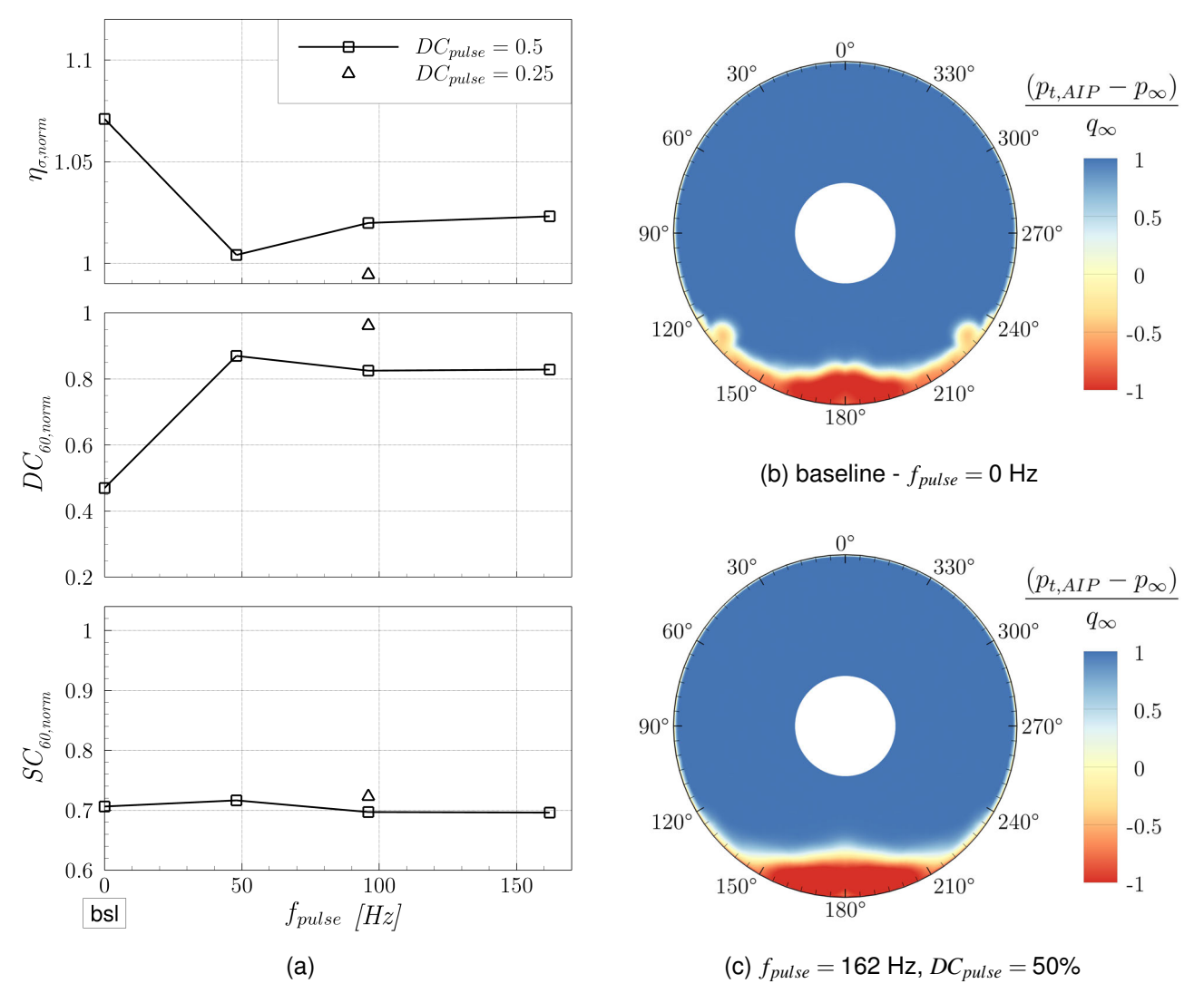


Figure 11 – (a) Results of the variation of temporal AFC characteristics; polar diagram of the time-averaged non-dimensional total pressure at the AIP of (b) the baseline configuration in continuous blowing mode; and (c) in pulsed blowing mode with a pulse frequency $f_{pulse} = 162 \text{ Hz}$ and a duty cycle $DC_{pulse} = 50\%$.

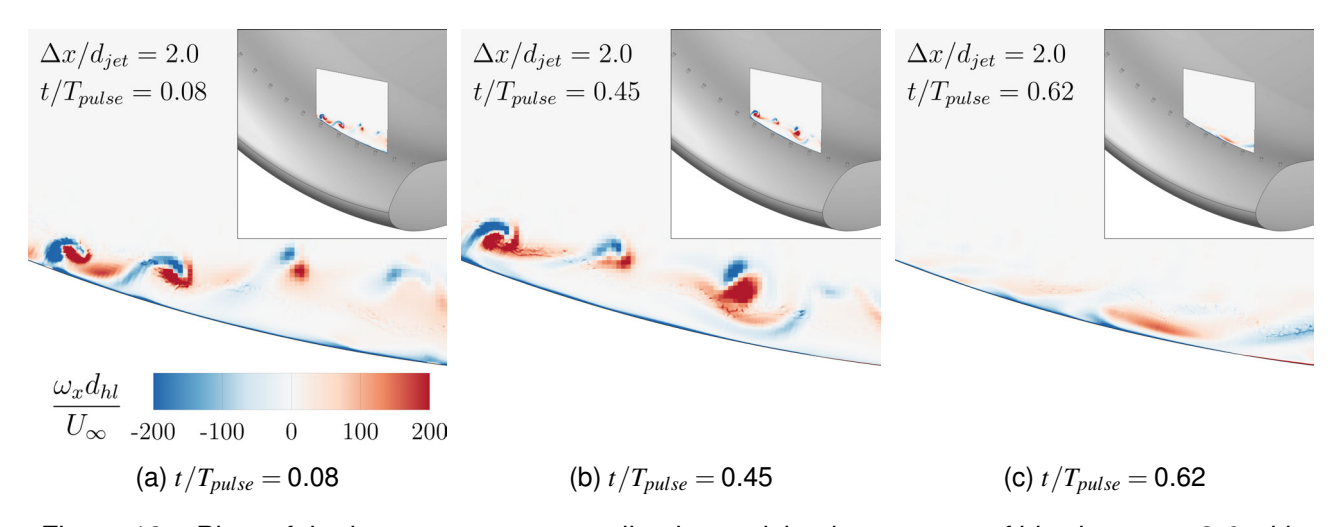


Figure 12 – Plots of the instantaneous normalized x-vorticity downstream of blowing ports 3-6 with $f_{pulse} = 162$ Hz and $DC_{pulse} = 50\%$ at three different cycle times.

clean case. On the other hand, the swirl coefficient $SC_{60,norm}$ at a duty cycle of 25% is only slightly higher than the value at 50%.

Upon closer examination of the polar diagrams in Fig. 11b and Fig. 11c, it is apparent that the underperformance of pulsed blowing is primarily attributed to increased pressure loss in the lower inlet section. The pulsed blowing mode at $f_{pulse} = 162$ Hz can suppress recirculation zones of the baseline configuration at circumferential angles of 130° and 230°. However, the AFC system exhibits poor efficiency in the 60° segment from 150° to 210°. The analysis of the vorticity at different cycle time gives insights into the reasons for the limited ability to prevent large scale flow separation in pulsed blowing mode. Similar to Fig. 9b, Figure 12 displays the normalized vorticity at two jet diameters downstream of port 3-6 at times $t/T_{pulse} = 0.08$, 0.45 and 0.62 of a pulse $T_{pulse} = 1/f_{pulse}$. The pulse frequency in Fig. 12 is again $f_{pulse} = 162$ Hz at a duty cycle of 50%. A time-controlled inlet boundary condition acts as a numerical valve, which opens at $t/T_{pulse} = 0.0$ and closes again at $t/T_{pulse} = 0.5$. The vorticity at $t/T_{pulse} = 0.08$ in Figure 12a indicates that vortex pairs are starting to form at the two outer ports, 5 and 6. Comparing the shape of the vortex pairs with the time-averaged data in Figure 9b, an increased circumferential cross-flow can be observed near the wall, impacting the CVPs. A similar scenario unfolds at time $t/T_{pulse} = 0.45$. At time $t/T_{pulse} = 0.62$, the valves have closed, and the vortex pairs in Fig. 12c disappear completely. A periodic pattern can be observed in which the recirculation zone repeatedly overflows the inner blowing ports. The strong circumferential cross-flow at the ports generated by the recirculation zone prevents the formation of well-formed and stable CVPs. The use of smaller pulse frequencies also shows a similar behavior, although the absolute pulse duration increases. Therefore, continuous blowing is the most promising operating mode for the tested conditions. A comparison of the inlet performance metrics of the best pulsed blowing configuration over the clean case yields an improvement of 2.3% in the total pressure coefficient η_{σ} , a 17.2% improvement in the distortion coefficient DC_{60} , and a 30.4% improvement in the swirl coefficient SC_{60} .

5. Conclusion

In this paper, an active flow control system was implemented on a short-inlet UHBR engine nacelle. The present research aims to achieve acceptable inflow conditions despite the short inlet length, even under off-design conditions, and thereby counteracting the drag and weight penalties of UHBR engine nacelles. A wind tunnel model will be designed based on the findings of this numerical study, which is why the primary purpose was not to closely simulate actual flight conditions. The AFC system was tested on the inlet of a generic, axisymmetric UHBR engine nacelle, which was conceptualized as a flow-through nacelle. The AFC system consisted of circular blowing ports near the inlet throat, injecting additional mass flow into the main inlet flow. Following the typical flow topology of jets in cross-flow, counter-rotating vortex pairs were expected to form behind the blowing ports. A URANS approach provided sufficient spatial resolution of the basic phenomena at a stalling inlet, while a scale-resolving SAS model was used for the more in-depth analysis of the unsteady temporal flow features. The inlet performance was assessed using the total pressure coefficient η_{σ} , the distortion coefficient DC_{60} , and the swirl coefficient SC_{60} . Analysis of the clean reference configuration without AFC found that large-scale inlet separation starts at an angle of attack of 26°. The selected off-design use-case scenario for the AFC system involved an angle of attack of $\alpha=29^{\circ}$ at a Mach number of $Ma_{\infty} = 0.15.$

Evaluating a promising baseline AFC configuration in continuous blowing mode showed significant improvements in inlet performance data compared to the clean configuration. The total pressure coefficient η_{σ} was enhanced by 7.1%, the distortion coefficient DC_{60} improved by 53.0%, and the swirl coefficient SC_{60} by 29.4%. Given a proper choice of parameters, distinct pairs of counter-rotating vortices form downstream of each jet. Further, it was found that vortex formation is favored when blowing is performed perpendicular to the local surface and ports are placed slightly downstream of the inlet throat. The variation of several AFC design parameters in continuous blowing revealed that the x-position along the inlet and the jet velocity are most sensitive to the system's efficiency. AFC in pulsed blowing mode turned out to be less efficient, as the periodic disruption of the jet prevents the formation of stable vortex pairs. Therefore, this numerical study indicates that more appropriate blowing strategies may exist for the pulsed blowing mode.

The following steps in this research project are the manufacturing of a well-equipped wind tunnel model. The use of 3D printing processes on the components of the AFC module, where the blowing ports are integrated, continues to provide sufficient design flexibility. Experimental campaigns will offer a profound validation database for further numerical investigations of AFC on engine inlets.

Contact Author Email Address

mailto: stefan.hayboeck@tum.de

Acknowledgments

The funding of this work by the BMWK within the LuFo VI-2 project AKTIVER (Aktive Strömungsbe-einflussung in Verdichterkomponenten künftiger Flugantriebe, FKZ: 20E2113A) is gratefully acknowledged. Further, the authors want to thank ANSYS for providing the simulation software used for this work. The authors gratefully acknowledge the Gauss Centre for Supercomputing e.V. (www.gauss-centre.eu) for funding this work by providing computing time on the GCS Supercomputer SuperMUC-NG at Leibniz Supercomputing Centre (www.lrz.de) and for providing additional computing time on its Linux cluster.

Copyright Statement

The authors confirm that they, and/or their company or organization, hold copyright on all of the original material included in this paper. The authors also confirm that they have obtained permission, from the copyright holder of any third party material included in this paper, to publish it as part of their paper. The authors confirm that they give permission, or have obtained permission from the copyright holder of this paper, for the publication and distribution of this paper as part of the ICAS proceedings or as individual off-prints from the proceedings.

References

- [1] Zimbrick R, and Colehour J. Investigation of very high bypass ratio engines for subsonic transport. *Journal of Propulsion and Power*, Vol. 6, No. 4, pp 490-496, 1990. doi: 10.2514/3.25461.
- [2] Peters A, Spakovszky Z, Lord W and Rose B. Ultra-short nacelles for low fan pressure ratio propulsors. *ASME Turbo Expo 2014: Turbine Technical Conference and Exposition*, Düsseldorf, GT2014, 26369, pp 1-15, 2014. doi: 10.1115/GT2014-26369.
- [3] Freeman C and Rowe A. Intake engine interactions of a modern large turbofan engine. *International Gas Turbine and Aeroengine Congress and Exhibition*, Indianapolis, 99-GT-344, pp 1-6, 1999. doi: 10.1115/99-GT-344
- [4] Lee K-B, Wilson M and Vahdati M. Effects of inlet disturbances on fan stability. *Journal of Engineering for Gas Turbines and Power*, Vol. 141, pp 1-11, 2019. doi: 10.1115/1.4042204
- [5] Piovesan T, Zachos P, MacManus D G and Sheaf C. Unsteady swirl distortion in a short intake under crosswind conditions. *AIAA SCITECH 2024 Forum*, Orlando, pp 1-16, 2024. doi: 10.2514/6.2024-1384
- [6] Williams D R and MacMynowski D G. Brief history of flow control. Fundamentals and applications of modern flow control. American Institute of Aeronautics and Astronautics, Reston, Virginia, 2009. doi: 10.2514/5.9781563479892.0001.0020
- [7] Gorton S, Owens L, Jenkins L, Allan B and Schuster E. Active flow control on a boundary-layer-ingesting inlet. *42nd AlAA Aerospace Sciences Meeting and Exhibit*, Reno, Nevada, pp 1-12, 2009. doi: 10.2514/6.2004-1203
- [8] Delot A-L, Garnier E and Pagan D. Flow control in a high-offset subsonic air intake. *47th AIAA/ASME/SAE/ASEE Joint Propulsion Conference & Exhibit*, San Diego, AIAA 2011-5569, pp 1-19, 2001. doi: 10.2514/6.2011-5569.
- [9] Garnier E. Flow control by pulsed jet in a curved S-duct: A spectral analysis. *AIAA Journal*, Vol. 53, No. 10, pp 2813-2827, 2015. doi: 10.2514/1.J053422.
- [10] Nambiar V and Pachidis V. Nacelle intake flow separation reduction at cruise condition using active flow control. *Propulsion and Power Research*, Vol. 11, No. 3, pp 337-352, 2022. doi: 10.1016/j.jppr.2022.07.005.
- [11] Margason R J. Analysis of the flow field of a jet in a subsonic crosswind. *Analytical Methods in Aircraft Aerodynamics*, Moffett Field, California, NASA SP-228, pp 683-702, 1969.
- [12] Margason R J. Fifty years of jet in cross flow research. *Computational and Experimental Assessment of Jets in Cross Flow*, Winchester, AGARD-CP-534, pp 1-41, 1993.

- [13] Godard G and Stanislas M. Control of a decelerating boundary layer. Part 3: Optimization of round jets vortex generators. *Aerospace Science and Technology*, Vol. 10, No. 6, pp 455-464, 2006. doi: 10.1016/j.ast.2005.11.005
- [14] Cambonie T, Gautier N and Aider J-L. Experimental study of counter-rotating vortex pair trajectories induced by a round jet in cross-flow at low velocity ratios. *Experiments in Fluids*, Vol. 54, No. 3, pp 1-13, 2013. doi: 10.1007/s00348-013-1475-9.
- [15] Guo R W and Seddon J. The swirl in an S-duct of typical air intake proportions. *Aeronautical Quarterly*, Vol. 34, No. 2, pp 99-129, 1983. doi: 10.1017/S0001925900009641
- [16] Seddon J. Understanding and countering the swirl in S-ducts: tests on the sensitivity of swirl to fences. *The Aeronautical Journal*, Vol. 88, No. 874, pp 117-127, 1984. doi: 10.1017/S0001924000020340
- [17] Schulze S, Kähler C and Radespiel R. On stalling flow-through nacelles and powered inlets at take-off conditions. *1st CEAS European Air and Space Conference*, Berlin, pp 3163-3171, 2007.
- [18] Christie R, Heidebrecht A and MacManus D. An automated approach to nacelle parameterization using intuitive class shape transformation curves. *Journal of Engineering for Gas Turbines and Power*, Vol. 139, No. 6, pp 1-19, 2017. doi: 10.1115/1.4035283
- [19] Christie R, Robinson M, Tejero F and MacManus D. The use of hybrid intuitive class shape transformation curves in aerodynamic design. *Aerospace Science and Technology*, Vol. 95, No. 105473, pp 1-13, 2019. doi: 10.1016/j.ast.2019.105473.
- [20] Kulfan B and Bussoletti J. "Fundamenta" Parameteric geometry representations for aircraft component shapes. *11th AIAA/ISSMO Multidisciplinary Analysis and Optimization Conference*, Portsmouth, Virginia, pp 547-591, 2006. doi: 10.2514/6.2006-6948
- [21] Egorov Y, Menter F R, Lechner R and Cokljat D. The scale-adaptive simulation method for unsteady turbulent flow predictions. part 2: application to complex flows. *Flow, Turbulence and Combustion*, Vol. 85, pp 139-165, 2010. doi: 10.1007/s10494-010-9265-4
- [22] Schulze S and Kähler C. Analysis of the flow in stalling engine inlet models with different visualization and measurement techniques. *Second Symposium "Simulation of Wing and Nacelle Stall"*, Braunschweig, pp 1-12, 2010.
- [23] Menter F R, Matyushenko A and Lechner R. Development of a generalized K-ω two-equation turbulence model. In: New Results in Numerical and Experimental Fluid Mechanics XII, Vol. 142, pp 101-109, 2020. doi: 10.1007/978-3-030-25253-3_10
- [24] Schulze S. Experimentelle Untersuchungen zur Wirbeldynamik am überziehenden Triebwerkseinlauf. Dissertation, Fakultät für Luft- und Raumfahrttechnik, Universität der Bundeswehr München, 2012.